The Astrophysical Journal, 994:56 (14pp), 2025 November 20 https://doi.org/10.3847/1538-4357/ae03a9

Imprints of Stellar Feedback on Magnetic Fields in the Iris Nebula NGC 7023

Ekta Sharma[1,2,11], Kate Pattle[3,11], Di Li[4,1,11], Chang Won Lee[5,6], Maheswar Gopinathan[7], Tao-Chung Ching[8], Mehrnoosh Tahani[9,10], and Shinyoung Kim[5]

[1] National Astronomical Observatories, Chinese Academy of Sciences, A20 Datun Road, Chaoyang District, Beijing 100012, People's Republic of China; ektasharma.astro@gmail.com, sharma.ekta@bao.ac.cn
[2] Physical Research Laboratory, Navrangpura, Ahmedabad, Gujarat 380009, India
[3] Department of Physics and Astronomy, University College London, Gower Street, London WC1E 6BT, UK; k.pattle@ucl.ac.uk
[4] New Cornerstone Science Laboratory, Department of Astronomy, Tsinghua University, Beijing 100084, People's Republic of China; dili@mail.tsinghua.edu.cn
[5] Korea Astronomy & Space Science Institute, 776 Daedeokdae-ro, Yuseong-gu, Daejeon, Republic of Korea
[6] University of Science and Technology, Korea (UST), 217 Gajeong-ro, Yuseong-gu, Daejeon 34113, Republic of Korea
[7] Indian Institute of Astrophysics, Koramangala II Block, Bangalore 560 034, India
[8] National Radio Astronomy Observatory, 1003 Lopezville Road, Socorro, NM 87801, USA
[9] Department of Physics & Astronomy, University of South Carolina, Columbia, SC 29208, USA
[10] Kavli Institute for Particle Astrophysics & Cosmology (KIPAC), Stanford University, Stanford, CA 94305, USA
Received 2025 January 20; revised 2025 August 5; accepted 2025 September 3; published 2025 November 13

Abstract

We present 850 μm polarized continuum observations carried out using SCUBA-2/POL-2 on the James Clerk Maxwell Telescope toward a reflection nebula, NGC 7023. The nebula is powered by the Herbig Ae Be star HD 200775 and also forms a *hub* in the hub-filament cloud, LDN 1172/1174. We detect submillimeter emission to the north and east of the location of the central star. The magnetic field (B-field) morphology is found to be curved and follows the clump morphology. The comparison of the B-field morphology at the clump scales (~0.02 pc) derived using POL-2 data with that of the envelope scale (~0.5 pc) derived using archival Planck/optical polarimetric observations suggests that the field lines are not preserved from envelope to clump scales. We suggest that this reordering of the magnetic field lines could be due to the interaction with the already evolved high-velocity outflow gas around the central star, which hints at the presence of outflow feedback. We estimated a B-field strength of 179 ± 50 μG in the starless core, and 121 ± 34 μG and 150 ± 42 μG in the protostellar cores, using the N_2H^+ (1–0) line observed with the 13.7 m single-dish telescope at the Taeduk Radio Astronomy Observatory (TRAO). The stability analysis gives magnetically subcritical values, while the magnetic, gravitational, and outflow kinetic energies are roughly balanced. Our study unveils the first possible evidence for magnetic field lines being shaped by outflow feedback in the vicinity of a photodissociation region driven by an intermediate-mass, pre-main-sequence star.

Unified Astronomy Thesaurus concepts: Star formation (1569); Molecular clouds (1072); Interstellar magnetic fields (845); Polarimetry (1278); Stellar feedback (1602)

1. Introduction

Magnetic fields (B-fields) play an important role in a broad range of astrophysical processes, ranging from regulating the star formation rate in the Milky Way (M. R. Krumholz & C. Federrath 2019) to the evolution of galaxies (R. Beck 2015). Given their omnipresence across all the scales of the interstellar medium (ISM), the magnetic fields affect different stages of star formation (R. M. Crutcher 2004; K. Pattle et al. 2023), i.e., the formation of filamentary structures (J. D. Soler et al. 2013), their fragmentation into cores (T.-C. Ching et al. 2022), and supporting the cores against the gravitational collapse (D. Ward-Thompson et al. 2000; E. Sharma et al. 2022). However, how the magnetic fields influence these dense structures in the presence of stellar feedback remains an open question.

Stellar feedback driven by massive stars ($M > 8$ $M_\odot$) affects the surrounding gas through photoionization and creates ionized atomic hydrogen regions (H II; H. Zinnecker & H. W. Yorke 2007), which create shocks as they expand into their surroundings (F. Motte et al. 2018). Intermediate-mass stars ($2 \leqslant M/M_\odot \leqslant 8$), the lower-mass counterparts of massive stars, cannot create extended H II regions due to their lower luminosities ($5 \leqslant L_{\rm bol}/L_\odot \leqslant 10^4$; F. Palla & S. W. Stahler 1993), yet drive feedback through the formation of photodissociated regions (PDRs). The pre-main-sequence stars in the previously mentioned mass range are mainly T-Tauri or Herbig Ae/Be stars. The associated PDRs, bounding the H II regions, are predominantly neutral atomic structures created by the interaction of ultraviolet radiation with molecular gas (D. J. Hollenbach & A. G. G. M. Tielens 1997). The magnetic fields near H II regions have been characterized well and are found to exhibit diverse morphologies, e.g., complex in Monoceros R2 (J. Hwang et al. 2022), reordered in NGC 6334 (M. Tahani et al. 2023), or unaltered by the stellar feedback in ρ Oph A (J. Kwon et al. 2018; N. Lê et al. 2024). However, the magnetic fields around intermediate-mass stars are poorly constrained because only a handful of studies have covered the magnetic field strengths of the clouds in the vicinity of PDRs (K. Pattle et al. 2018; J. Hwang et al. 2023). A large amount of molecular gas fueling star formation resides in PDRs (T. Y. Steiman-Cameron et al. 1997). The lack of ionization fronts and their complex recombination processes in PDRs driven by intermediate-mass stars allows a simpler energetic analysis as compared to that in H II regions driven by high-mass stars, while investigating the magnetic fields under stellar feedback.

[11] Corresponding author.

Three-dimensional radiation magnetohydrodynamic simulations for the expansion of ionized regions in a uniform magnetized medium suggest that the B-field morphology in the surrounding natal cloud is compressed by the radiation from young stars (S. J. Arthur et al. 2011; J. Mackey & A. J. Lim 2011). As a result, the field lines are aligned parallel to the neutral gas layers due to their interaction with the H II regions or PDRs. This finding agrees well with several observational attempts for different extinction layers of the clouds, at smaller wavelengths (A. Pereyra & A. M. Magalhães 2007; A. Soam et al. 2017; Z. Chen et al. 2022) and longer wavelengths (K. Pattle et al. 2019; C. Eswaraiah et al. 2020), with the magnetic fields being aligned with ionization fronts.

Interstellar aspherical dust grains in the ISM are preferentially aligned with their major axes perpendicular to the local magnetic field orientation projected onto the plane-of-sky (L. Davis & J. L. Greenstein 1951; S. Chandrasekhar & E. Fermi 1953; A. Lazarian & T. Hoang 2007). Hence the thermal emission from dust grains is linearly polarized and can be used as an efficient tool to probe the magnetic fields of molecular clouds at submillimeter/millimeter wavelengths (R. M. Crutcher 2012). We have employed submillimeter polarization and molecular line emission in this work to investigate the role of magnetic fields at clump scales in the vicinity of PDRs triggered by an intermediate-mass star.

Nearby reflection nebulae are the best indicators of recent or ongoing star formation activity as the radiation field around the massive star heats the surrounding gas and modifies the chemistry of structures, making them illuminated (T. Y. Magakian 2003). We chose NGC 7023, a reflection nebula illuminated by an intermediate-mass star. This nebula hosts PDRs triggered by the central star, HD 200775, and a bipolar outflow (described in Section 2), making it an ideal laboratory for investigating the dynamical role of magnetic fields in dense cloud structures influenced by stellar feedback.

2. Target Selection: NGC 7023

The NGC 7023 (the Iris nebula; R.A.: $21^{h}01^{m}37^{s}$, decl.: $+68°09'48''$ [J2000]) is a reflection nebula located in the Cepheus Flare constellation at a distance of 340 pc (P. Saha et al. 2020). The spatial extent of the nebula in the plane-of-sky is 1.5 pc (angular extent of $\sim 15'$ in the east–west direction). The nebula hosts an intermediate-mass star HD 200775, which is a spectroscopic binary system of spectral type B3Ve-B5 (E. Alecian et al. 2008). The region is termed a "hub-filament" complex by P. C. Myers (2009), with NGC 7023 sitting at the location of the hub. The region holds the highest concentration of young stellar objects (YSOs) in all Cepheus Flare clouds (J. M. Kirk et al. 2009). This region contains PDRs (M. Köhler et al. 2014), high-density regions, and diffuse gas streamers seen in gas and dust emission maps. For the present study, we chose this particular region of the nebula because it is in the closest proximity to the central star and is expected to show possible signatures of stellar feedback. The magnetic field structure of NGC 7023 has been studied using starlight polarization at $\sim 0.6\,\mu$m using the Aries IMaging POLarimeter (AIMPOL) by P. Saha et al. (2021). The global magnetic fields are quite regular. With the high sensitivity of POL-2, we mapped the magnetic fields in this region, which has present feedback from an intermediate-mass star (see the solid black circle marked in Figure 1 [left panel]).

The paper is organized as follows. In Section 3, we describe our observations and the data reduction of the James Clerk Maxwell Telescope (JCMT) POL-2 and the molecular line observations using TRAO. In Section 4, we present the results of our 850 μm continuum polarization observations and the resulting magnetic field morphology toward the reflection nebula. We study the dust grain properties using the Ricean model on the obtained polarization fractions and also derive the magnetic field strength using the Davis–Chandrasekhar–Fermi method. In Section 5, we finally discuss our results and compare the magnetic field energy with the turbulent kinetic, gravitational, and outflow energies. Based on the results, we suggest an evolution scenario of the clump around the PDR. We finally summarize our results in Section 6.

3. Observations and Data Reduction

3.1. JCMT POL-2 Data

We observed the NGC 7023 region 34 times between 2021 August 7 and 2022 May 24 using the POL-2 polarimeter (P. Friberg et al. 2016) mounted on the Submillimetre Common-User Bolometer Array 2 (SCUBA-2; W. S. Holland et al. 2013) on the JCMT. The data were taken in a mixture of Band 1 ($\tau_{225\,\mathrm{GHz}} < 0.05$) and Band 2 ($0.05 < \tau_{225\,\mathrm{GHz}} < 0.08$) weather under project codes M21BP004 and M22AP012. Each observation consisted of a 31-minute POL-2-DAISY scan pattern.

The data were reduced using the *pol2map*[12] script recently added to the SMURF package in the *Starlink* software suite (E. L. Chapin et al. 2013). See K. Pattle et al. (2021) for a detailed description of the current POL-2 data reduction process. Instrumental polarization (IP) was corrected for using the "2019 August" IP model.[13] The 850 μm data were calibrated with a flux conversion factor (FCF) of 2795 mJy arcsec^{-2} pW^{-1} using the post–2018 June 30 SCUBA-2 FCF of 2070 mJy arcsec^{-2} pW^{-1} (S. Mairs et al. 2021), multiplied by a factor of 1.35 to account for additional losses in POL-2 (P. Friberg et al. 2016). POL-2 observes simultaneously at 850 μm and 450 μm, but we consider only the 850 μm observations in this work as the 450 μm data reduction process remains under development.

The pixel size of the final Stokes I, Q, and U maps is set to $4''$, the default and recommended pixel size for 850 μm SCUBA-2 data reduction (E. L. Chapin et al. 2013). To achieve better sensitivity, we then binned our output debiased polarization vector catalog to $8''$ pixels (approximately Nyquist-sampled) using the parameter *binsize* in the reduction pipeline. The average rms noise in Stokes Q, U, and I in the central $3'$ of the map on $8''$ pixels is 0.8 mJy beam^{-1}.

The observed polarized intensity is given by

$$PI' = \sqrt{Q^2 + U^2}. \quad (1)$$

We debiased this quantity using the modified asymptotic estimator (S. Plaszczynski et al. 2014; L. Montier et al. 2015),

$$PI = PI' - \frac{1}{2}\frac{\sigma^2}{PI'}\left(1 - e^{-\left(\frac{PI'}{\sigma}\right)^2}\right), \quad (2)$$

[12] http://starlink.eao.hawaii.edu/docs/sun258.htx/sun258ss73.html

[13] https://www.eaobservatory.org/jcmt/2019/08/new-ip-models-for-pol2-data/

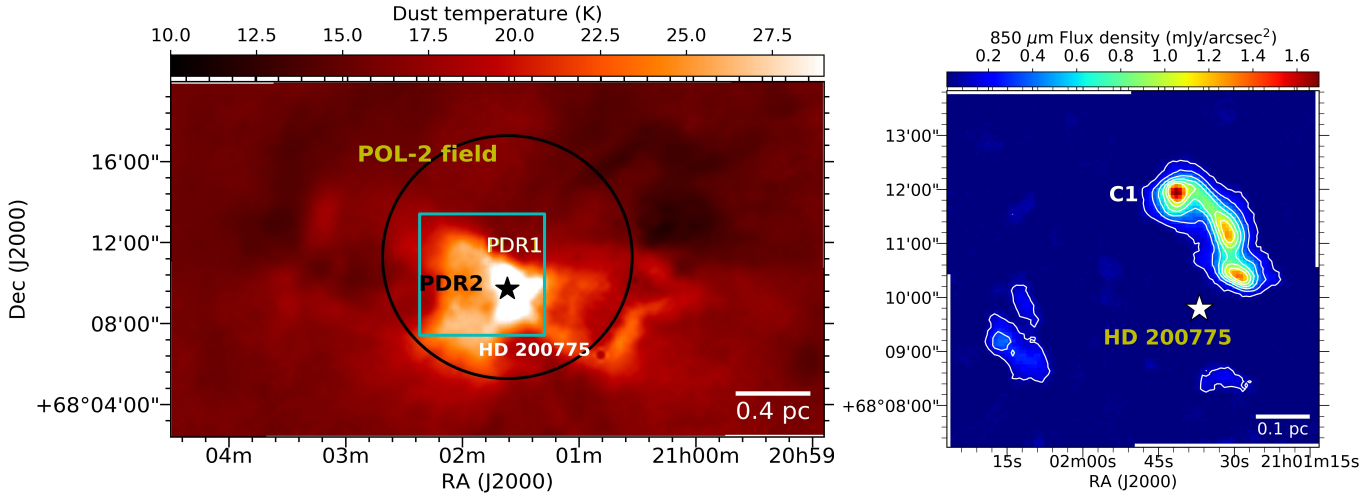

Figure 1. Left: dust temperature map of NGC 7023 derived from Herschel maps of L1172/1174 cloud (J. Di Francesco et al. 2020). The central star is marked in black with PDRs labeled. The solid black circle marks the POL-2 field of 6′ radius. The cyan box shows the area of interest that is considered in later figures. Right: SCUBA-2 850 μm Stokes I map obtained with our polarization observations. The clump C1 is labeled. The SCUBA-2 dust continuum emission contours in white range from 0.1 (10σ) to 1.1 mJy arcsec^{-2} in the intervals of 20σ, $\sigma = 0.01$ mJy arcsec^{-2}.

where σ^2 is the weighted mean of the variances σ_Q^2 and σ_U^2, and

$$\sigma^2 = \frac{Q^2\sigma_Q^2 + U^2\sigma_U^2}{Q^2 + U^2}, \quad (3)$$

calculated on a pixel-by-pixel basis. The debiased polarization fraction is given by $p = PI/I$.

The polarization angle is given by

$$\theta_p = 0.5 \arctan(U, Q). \quad (4)$$

We note that the polarization angles we detect are not true vectors, as they occupy a range in angle of 0°–180°. We nonetheless refer to our polarization angle measurements as vectors for convenience to keep consistency with the general convention used in this field (IAU 1973). Throughout this work, we assume that dust grains are aligned with their major axis perpendicular to the magnetic field direction (e.g., B. G. Andersson et al. 2015), so that the plane-of-sky magnetic field direction can be inferred by rotating θ_p by 90°.

3.2. Molecular Line Data

We used molecular line data for N_2H^+ (1–0), CS (2–1), $C^{18}O$ (1–0), and ^{12}CO (1–0), observed using a 13.7 m single-dish telescope at TRAO,[14] in South Korea, from 2018 November to December. The observations were carried out as part of mapping the large cloud L1172/1174 using four tracers. We used the new receiver system, Second QUabbin Observatory Imaging Array-TRAO (SEQUOIA-TRAO), in the 85–115.6 GHz frequency range. The pointing accuracy was achieved to be $\leqslant 5''$ using a standard X Cygnus source in the SiO line. The back-end system with a fast Fourier transform spectrometer has 4096×2 channels at 15 kHz resolution ($\sim$0.05 km s^{-1} at 110 GHz). The spatial resolution was $47''$ at 109.7821734 GHz, and the final velocity resolution for the data was adjusted to be 0.1 km s^{-1}. The system temperature (T_{sys}) was 500–700 K during the observations. The typical rms noise (T_A^*) is $\sim$0.09 K for $C^{18}O$ and $\sim$0.3 K for ^{12}CO (1–0) with a channel of 0.1 km s^{-1}. The achieved rms noise is $\sim$0.06 K for N_2H^+ (1–0) and 0.1 K for CS (2–1), line with a channel of 0.06 km s^{-1}. The rest frequencies used in our observations for CS (2–1) and N_2H^+ (JF1F = 101 – 012) are 96.412953 GHz and 93.176258 GHz, respectively (C. W. Lee et al. 2001). We used the astronomical software package Gildas/CLASS[15] for data reduction.

We mainly used the dense gas tracer N_2H^+ for the estimation of magnetic field strength in NGC 7023. The N_2H^+ (1–0) line (critical density, $n_{crit} \sim 10^5$ cm^{-3}; Y. L. Shirley 2015) traces dense gas, particularly in the prestellar phase (P. Caselli et al. 2002), and its intensity closely matches with the submillimeter dust emission (J. di Francesco et al. 2007). However, other dense gas tracers such as $C^{18}O$ (1–0) and CS (2–1) are also often used in the magnetic field analysis. Our observational setup allows for the simultaneous observation of these lines. The $C^{18}O$ ($n_{crit} \sim 10^3$–10^4 cm^{-3}) and CS (2–1) ($n_{crit} \sim 1.3 \times 10^5$ cm^{-3}; Y. L. Shirley 2015) trace dense gas in the filaments and prestellar cores (C. W. Lee et al. 2001), respectively. Hence we used all three of them to investigate the variations in magnetic field strengths using N_2H^+, $C^{18}O$, and CS (2–1) lines (see the Appendix). The ^{12}CO line is a diffuse gas tracer ($n_{crit} \sim 100$ cm^{-3}), and we utilized the line emission to estimate the outflow parameters in this work.

4. Results

4.1. Magnetic Field Morphology

Figure 1 shows the dust temperature map of NGC 7023 on the left and the detected 850 *mum* Stokes I map obtained from SCUBA-2 observations of the observed region toward NGC 7023 on the right. The location of PDRs is labeled. Investigating the structure and physical conditions of the PDRs is important for understanding the effect of stellar feedback. The outflow has carved out a biconical cavity and created the PDRs, marked as PDR 1 and PDR 2 (M. Köhler et al. 2014), triggered as a result of HD 200775 (B3Ve-B5 spectral type).

[14] https://trao.kasi.re.kr/

[15] http://www.iram.fr/IRAMFR/GILDAS/

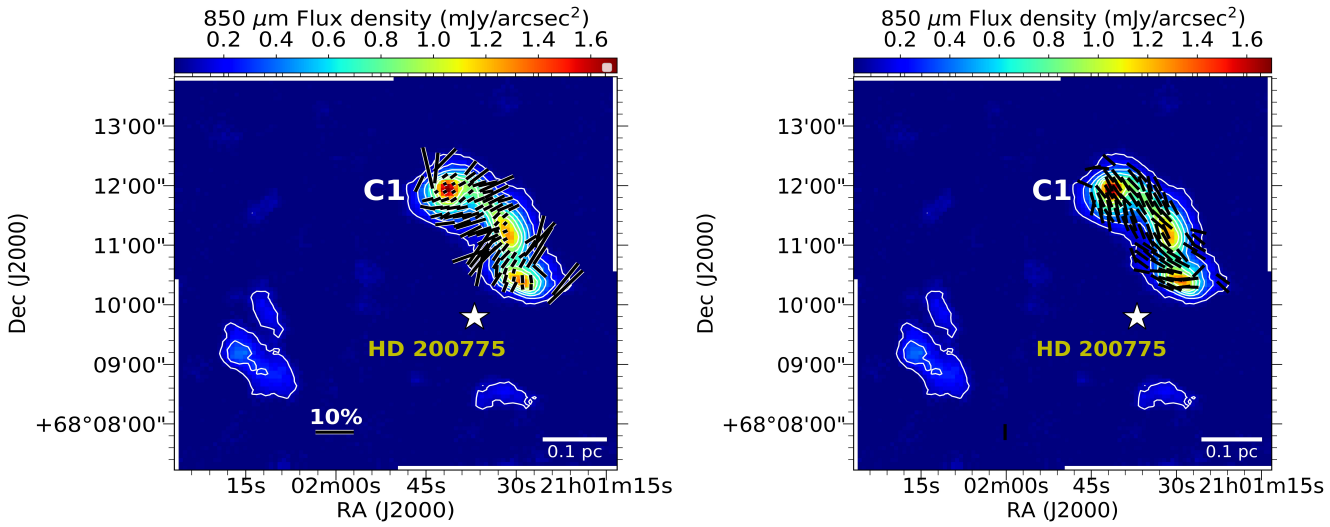

Figure 2. Left: the POL-2 dust polarization map at 850 μm toward NGC 7023 reflection nebula near the Herbig Ae Be star, HD 200775. The background image shows the Stokes I intensity. The black lines show the polarization angles, and the degree of polarization in their length is proportional to polarization percentages. A reference vector with a polarization percentage of 10% is shown. Right: the magnetic field map toward NGC 7023 with equal length vectors that have been rotated by 90° to trace the plane-of-sky magnetic field direction.

The solid black circle marks the region that we observed with POL-2, and the cyan box represents the region of interest covered in further analysis. The right panel shows the obtained SCUBA-2 dust emission map, with the areas of emission detected at 10σ or higher ($\sigma = 0.01$ mJy arcsec^{-2}) outlined with white contours. We find three main regions of emission, one toward the north (identified as clump C1) and a small extent toward the east and the south. The detected emission correlates with the position of marked PDRs, which are present toward dense gas structures' rims.

Figure 2 (left) shows the distribution of polarization angles toward the clump C1. The vectors were selected based on $p_{db}/\delta p > 3$, $I/\delta I > 5$, and $\delta\theta < 10°$, where the first and third conditions are degenerate considering Serkowski's approximation, $\delta\theta \approx 28.65 \times \delta p/p$ (K. Serkowski 1962). The vectors in the regions to the east and south of the star HD 200775 do not satisfy the selection criteria, and so we consider magnetic fields in region C1 only. The polarization fraction shows a decrease toward the high-intensity regions. This depolarization may result from a combination of field tangling and the loss of grain alignment at elevated optical extinctions (B. G. Andersson et al. 2015). At lower visual extinctions (A_V), dust grains tend to align their minor axis along the direction of the local magnetic field (L. Davis & J. L. Greenstein 1951; D. C. B. Whittet et al. 2008; F. O. Alves et al. 2014). However, as the optical depth increases, dust grains tend to lose their alignment due to the absence of a non-isotropic radiation field, which is crucial in the spinning of asymmetrical dust grains in accordance with the radiative alignment torque (RAT) theory of grain alignment (A. Lazarian & T. Hoang 2007). We quantify the efficiency of grain alignment in more detail in Section 4.4. In the right panel of Figure 2, we show the distributions of magnetic field orientation (black lines), which are obtained by rotating the polarization angles by 90°. The B-fields exhibit a preferred orientation of 35°E of N and align with the clump morphology. In the next section, we further quantify the correlation of clump morphology with the B-field orientation.

4.2. Comparison of Filament and Magnetic Field Orientation

As mentioned in the previous section, the magnetic field orientation inferred from POL-2 data is curved and runs along the clump morphology. This clump shows a high aspect ratio and hosts three cores, which are protostellar and starless (K. Pattle et al. 2017). Therefore, we considered this a filament and extracted the filament orientation using the Filfinder algorithm (E. W. Koch & E. W. Rosolowsky 2015). We used a global threshold of 0.6 mJy arcsec^{-2} and an adaptive threshold of 8 pixels on the SCUBA-2 map. We used a size threshold of 200 square pixels to extract filaments with lengths down to 0.3 pc. Figure 3 shows the high-density filament in black derived using the Filfinder algorithm. Three high-density cores are marked toward the clump C1 in 850 μm emission (magenta triangles). The dust emission properties of these cores have been studied by K. Pattle et al. (2017), and hereafter we adopt their names: P17 21 for starless, P17 23 for protostellar with a class I source, and P17 24 for protostellar with a class II source. Since the region shows curved morphology, we examined the polarization angles of vectors that are the nearest neighbors to the filament. Further, we divided the filament into three regions—I, II, and III—to compare the orientation of the filament segment in each region and the average B-field orientation. The regions are shown by solid green circles in Figure 3. The average magnetic field orientation within the I region is $\langle\theta_B^{\rm I}\rangle = 26.^{\circ}4 \pm 26.^{\circ}0$, and the orientation of the filament segment is $\theta_f^{\rm I} = 52°$. The orientation of the filament and magnetic fields is taken from north toward east. The average magnetic field orientation in region II $\langle\theta_B^{\rm II}\rangle = 35° \pm 14°$, and $\theta_f^{\rm II} = 38°$. In region III, $\langle\theta_B^{\rm III}\rangle = 39° \pm 53°$ and $\theta_f^{\rm III}$ is 36°, around core P17 24. The mean orientation of the magnetic fields and the filament segments match well within all three regions. The calculated uncertainty of the magnetic field orientations is the standard deviation (1σ) of the sample. However, the dispersion of B-field orientations with respect to their mean in region III is higher, and thus the individual vectors have higher offsets with respect to filament orientation, as compared to those in regions I and II.

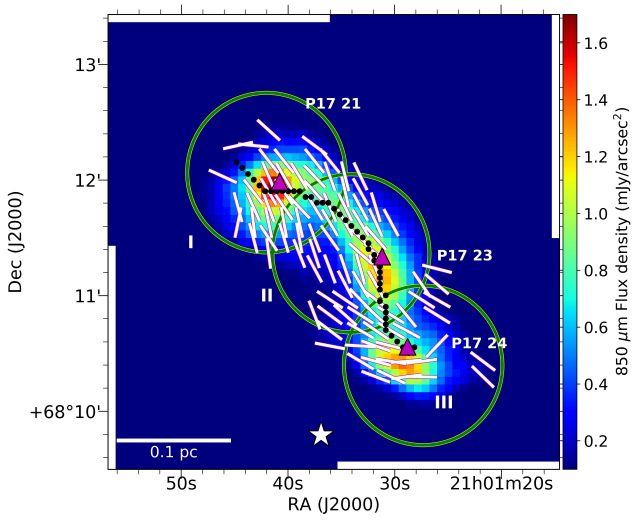

Figure 3. Extracted filament shown as a black dotted line overplotted on the SCUBA-2 image, with magnetic field lines shown in white. The magenta triangles show three cores, labeled as P17 21, P17 23, and P17 24. The names were adopted from K. Pattle et al. (2017). The circles show the regions I, II, and III, chosen to calculate the average magnetic field around the three cores.

4.3. Comparison with Large-scale Magnetic Field Structure from Planck and Starlight Polarization

The Planck polarization data at 353 GHz (850 μm) are used to study the large-scale magnetic fields around NGC 7023 at the Planck resolution of 5′ (0.5 pc). P. Saha et al. (2021) have studied the large-scale magnetic field using high-resolution starlight polarization measurements at optical wavelengths, as well as the Planck data. Figure 4 shows the magnetic field vectors from optical data (in yellow) and Planck (in magenta) overplotted on a Herschel column density image. In the zoomed-in version of the small inset marked with a cyan box on the left image, we show the POL-2 vectors (red lines) overplotted on the SCUBA-2 850 μm emission map. The optical polarization and the Planck polarization vectors agree well with each other, whereas the structure of the magnetic fields is quite different at clump scales. The diffuse regions on the western and eastern sides of HD 200775 show a fairly regular magnetic field with a northwest–southeast orientation following the diffuse structures. The same magnetic fields at larger scales are broadly perpendicular to the major axis of the high-density structure on the eastern side and parallel to that on the western side. This is similar to what we expect from the bimodal distribution of magnetic fields (J. D. Soler et al. 2013; Planck Collaboration et al. 2016). In contrast, the POL-2 vectors appear reordered at smaller scales and follow the curvature of the clump.

Figure 5 shows the distribution of polarization angles obtained with POL-2 in green. The mean polarization angle $\langle\theta_{\rm POL2}\rangle = 46^\circ \pm 30^\circ$. The distribution of Planck and optical polarization angles is shown in gray and red histograms, respectively. The mean values from both the data sets are $\langle\theta_{\rm Planck}\rangle = 148^\circ \pm 26^\circ$ and $\langle\theta_{\rm optical}\rangle = 144^\circ \pm 19^\circ$. The uncertainty in the three data sets is their respective standard deviation (1σ) of the sample. The magnetic field structure inferred from both Planck and optical polarization follows a similar distribution. The dispersion of POL-2 data is broader, and notably, the morphology of the magnetic field traced by POL-2 is completely different from the large-scale field orientation, which is well aligned with the diffuse low-column-density structures. This difference in orientation between large and small scales suggests that the cloud-scale B-field is not preserved in dense gas.

4.4. Grain Alignment Properties

Polarized dust emission observations typically show a power-law dependence, $p \propto I^{-\alpha}$, where $0 \leqslant \alpha \leqslant 1$ (D. C. B. Whittet et al. 2008; T. J. Jones et al. 2015). A steeper index (higher α) indicates either poorer grain alignment with respect to the magnetic field or more variation of the magnetic field direction along the line of sight (LOS). Note that $\alpha = 0$ indicates grains are consistently aligned throughout the LOS, while $\alpha = 1$ implies complete randomization of either grain alignment or magnetic field direction along the LOS (K. Pattle et al. 2019).

We measured α using the method described by K. Pattle et al. (2019), in which we assume that the underlying relationship between p and I can be parametrized as

$$p = p_{\sigma_{\rm QU}} \left(\frac{I}{\sigma_{\rm QU}} \right)^{-\alpha}, \tag{5}$$

where $p_{\sigma_{\rm QU}}$ is the polarization fraction at the rms noise level of the data $\sigma_{\rm QU}$ and α is a power-law index in the range $0 \leqslant \alpha \leqslant 1$. We fitted the relationship between I and observed non-debiased polarization fraction p' with the mean of the Ricean distribution of observed values of p that could arise from Equation (5) in the presence of Gaussian rms noise $\sigma_{\rm QU}$ in Stokes Q and U,

$$p'(I) = \sqrt{\frac{\pi}{2}} \left(\frac{I}{\sigma_{\rm QU}} \right)^{-1} \mathcal{L}_{\frac{1}{2}} \left(-\frac{p_{\sigma_{\rm QU}}^2}{2} \left(\frac{I}{\sigma_{\rm QU}} \right)^{2(1-\alpha)} \right), \tag{6}$$

where $\mathcal{L}_{\frac{1}{2}}$ is a Laguerre polynomial of order $\frac{1}{2}$. See K. Pattle et al. (2019) for a derivation of this result. We restricted our data set to the central 3′ diameter region over which exposure time, and thus rms noise, is approximately constant (P. Friberg et al. 2016).

The relationship between p' and I in NGC 7023 is shown in Figure 6. By fitting Equation (6) to the data, we measure a best-fit index of $\alpha = 0.62 \pm 0.04$. This suggests that in our observations of NGC 7023, grains remain fairly well aligned even at the highest column densities. A power-law index of 0.5 implies a linear decrease in the polarization fraction, suggesting that the dust grain alignment decreases linearly with the depth into the cloud. This trend of decreasing polarization as a function of increasing Intensity has also been seen in other molecular clouds (J. Kwon et al. 2018; A. Soam et al. 2018; K. Pattle et al. 2019; W. Kwon et al. 2022). This could result from decreasing radiation fields and increasing gas density or larger grain sizes in dense regions (T. Hoang et al. 2021). However, our obtained value (~0.6) is not much steeper than expected for a linear loss of alignment. This suggests that the grain alignment is being maintained relatively well in this region, perhaps due to the strong asymmetric interaction of the C1 clump with the radiation field of HD 200775. There are also two protostellar cores with Class I (P17 23) and Class II protostars (P17 24) embedded in the high-density clump C1 (K. Pattle et al. 2017). T. Henning et al. (2001) has found a similar result for CB 54 and DC 253-1.6 with α as 0.64 and 0.55, respectively. Both of these have embedded sources,

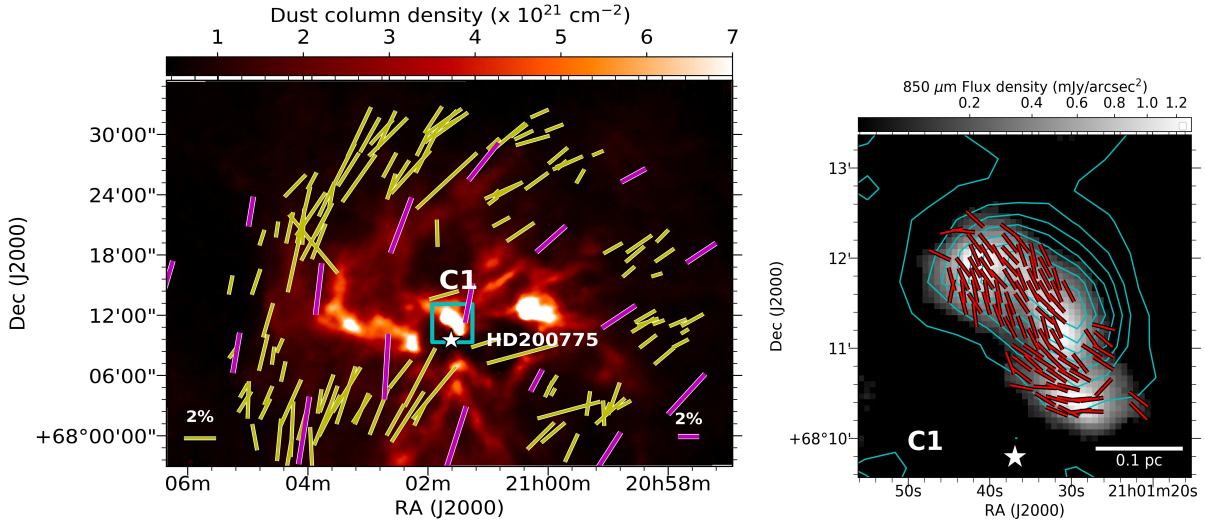

Figure 4. Left: Herschel dust column density map of NGC 7023. The white star marks the position of the intermediate-mass star HD 200775. The magenta lines show the magnetic fields derived from Planck polarization data, and the yellow lines show the magnetic field lines measured using optical polarization vectors (P. Saha et al. 2021). Right: SCUBA-2 850 μm Stokes I map toward C1. The zoomed-in region is marked with a cyan box in the main image. The integrated intensity contours of N_2H^+ (1–0) in cyan are in the range from 0.5 to 1.4 K km s^{-1} (step size ~0.1 K km s^{-1}). Red vectors show our POL-2 observations toward C1 with $p_{db}/dp > 3$.

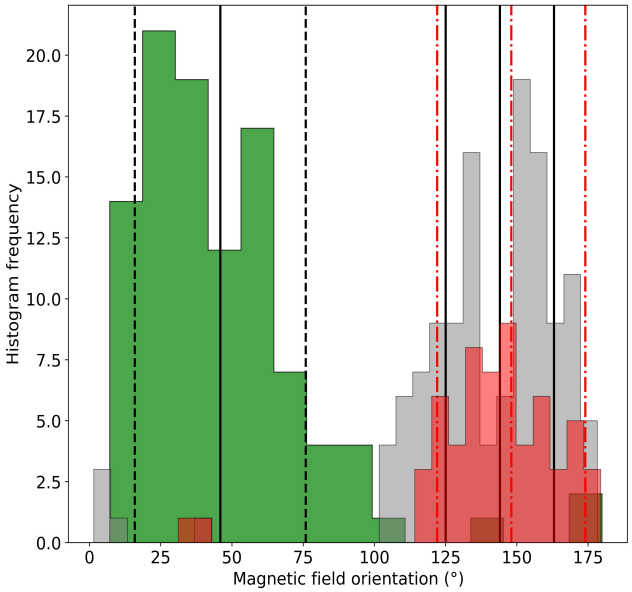

Figure 5. The distribution of polarization angles, rotated by 90° to infer the magnetic field orientations obtained using JCMT POL-2, is shown in green. The B-field orientations from optical R-band P. Saha et al. (2021) and from Planck polarization data (rotated by 90°) are plotted in gray and red, respectively. The black and red vertical lines around the R-band (~0.6 μm) and Planck distribution are the mean magnetic field direction with their range of dispersion.

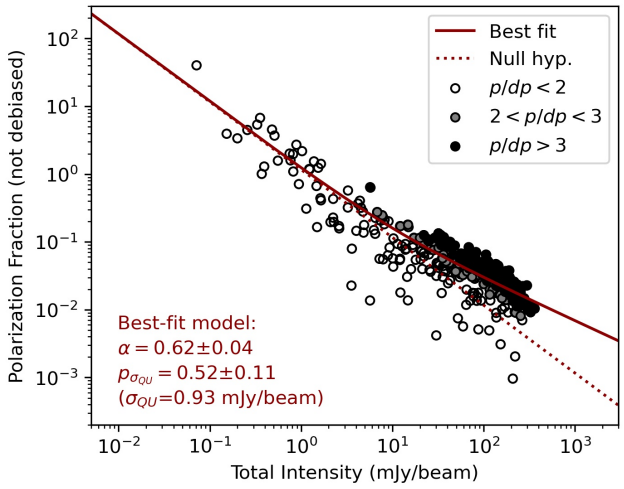

Figure 6. Non-debiased polarization fraction as a function of Stokes I intensity, fitted with a single-power-law distribution and a Ricean noise model, as described in the text. All data points in the central 3′-diameter region of the image are shown and fitted. Those at $p/dp > 2$ are shaded in gray; those at $p/dp > 3$ are shaded in black. The best-fit model, with a power-law index $\alpha = 0.62 \pm 0.04$, is shown as a solid maroon line. The behavior in the absence of true polarized signal, $p' = \sqrt{\pi/2}\,(I/\sigma_{QU})^{-1}$, is shown as a dashed maroon line.

which may be responsible for maintaining the RAT. In opposition to this effect, the presence of either multiple magnetic field components along the LOS or a complex magnetic field structure on scales smaller than the beam may be responsible for depolarization toward the high-density regions.

4.5. Magnetic Field Strength

We estimated the magnetic field strengths in NGC 7023 using the Davis–Chandrasekhar–Fermi (hereafter DCF) method (L. Davis 1951; S. Chandrasekhar & E. Fermi 1953), which assumes that perturbations in the magnetic field angle from the mean direction of the field arise from small-scale nonthermal motions of the gas (i.e., the perturbations in the magnetic fields are Alfvénic). The conventional methods of estimating magnetic field strength using DCF relation include effects from the turbulent eddies averaged along the LOS, and these methods tend to overestimate the mean plane-of-sky magnetic field by a factor of $\sqrt{N_{\rm turb}}$ (J. Cho & H. Yoo 2016), where $N_{\rm turb}$ is the number of independent turbulent cells along the LOS. Therefore, J. Cho & H. Yoo (2016) proposed a modified DCF method

for the calculation of the plane-of-sky magnetic field strength,

$$B_{\rm pos} = Q\sqrt{4\pi\rho}\left(\frac{\delta v_c}{\delta\theta}\right), \quad (7)$$

where δv_c is the centroid velocity dispersion of the region in km s^{-1}, ρ is the gas density in g cm^{-3}, and $\delta\theta$ is the polarization angle dispersion over the selected region. Q is a constant of order unity ($0.7 \leqslant Q \leqslant 1$) derived through numerical simulations, as suggested by J. Cho & H. Yoo (2016). We further write the ratio $(\delta v_c/\delta v)$ as

$$(\delta v_c/\delta\theta) = (\delta v_c/\delta v) \times (\delta v/\delta\theta), \quad (8)$$

where δv is the average velocity dispersion obtained using molecular line data. The authors found that the ratio $(\delta v_c/\delta\theta)$ is proportional to $1/\sqrt{N_{\rm turb}}$, and Equation (8) can be written as

$$(\delta v_c/\delta\theta) = (1/\sqrt{N_{\rm turb}}) \times (\delta v/\delta\theta). \quad (9)$$

Putting this ratio in Equation (13), the plane-of-sky magnetic field strength becomes

$$B_{\rm pos} = \sqrt{4\pi\rho} \times \frac{\delta v}{\delta\theta} \times \frac{1}{\sqrt{N_{\rm turb}}}. \quad (10)$$

4.5.1. Structure Function

We estimated magnetic field strengths using the R. H. Hildebrand et al. (2009) implementation of the DCF method (L. Davis 1951; S. Chandrasekhar & E. Fermi 1953), in which the ordered and turbulent components of the magnetic field are separated using a structure-function-based approach.

We calculated the difference in polarization angle among individual pairs of polarization segments, $\Delta\theta(l) \equiv \theta(x) - \theta(x + l)$, where $\theta(x)$ is the polarization angle of a segment at position x and $\theta(x + l)$ is the polarization angle of a segment separated from x by a distance l. If the number of pairs is given by $N(l)$, the angular dispersion function is then given by

$$\langle\Delta\theta^2(l)\rangle^{1/2} \equiv \left[\frac{1}{N(l)}\sum_{i=1}^{N(l)}\Delta\theta(l)^2\right]^{1/2}. \quad (11)$$

This can, at small l, be fitted with the quadratic function

$$\langle\Delta\theta^2(l)\rangle = b^2 + m^2l^2 + \sigma_M^2(l), \quad (12)$$

where ml arises from the ordered magnetic field (referred to as the large-scale field by R. H. Hildebrand et al. 2009), b is the turbulent dispersion about the mean magnetic field, and $\sigma_M(l)$ is the measurement uncertainty.

Figure 7 shows our structure function: $b = 17.^{\circ}0 \pm 1.^{\circ}3$ (0.30 ± 0.02 radians). The turbulent to large-scale magnetic field strength ratio is given by $b/\sqrt{2 - b^2}$. When the turbulent component of the magnetic field is much smaller than the ordered component (i.e., $b \ll 1$ rad, $b/\sqrt{2 - b^2} \rightarrow b/\sqrt{2}$), the DCF relation becomes

$$B_{\rm pos} = \sqrt{8\pi\rho} \times \left(\frac{\sigma_{nt}}{b}\right) \times \frac{1}{\sqrt{N_{\rm turb}}}, \quad (13)$$

where $B_{\rm pos}$ is the plane-of-sky magnetic field strength, ρ is gas mass density, and σ_v is the average nonthermal velocity dispersion of the gas.

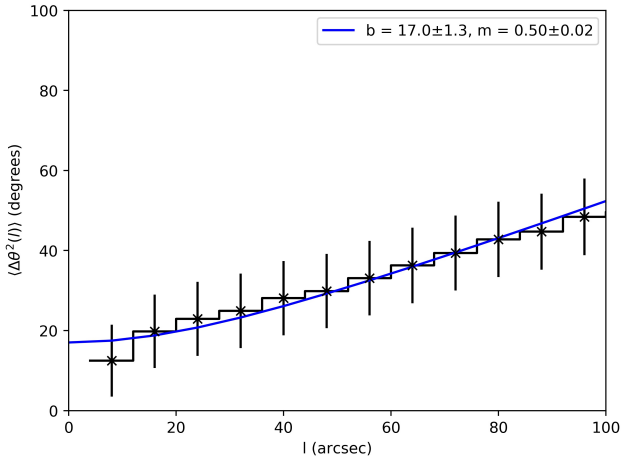

Figure 7. The angular dispersion function for the polarization angles obtained from the POL-2 data. The best-fit parameters were found by fitting Equation (12) and are shown in the top-right legend.

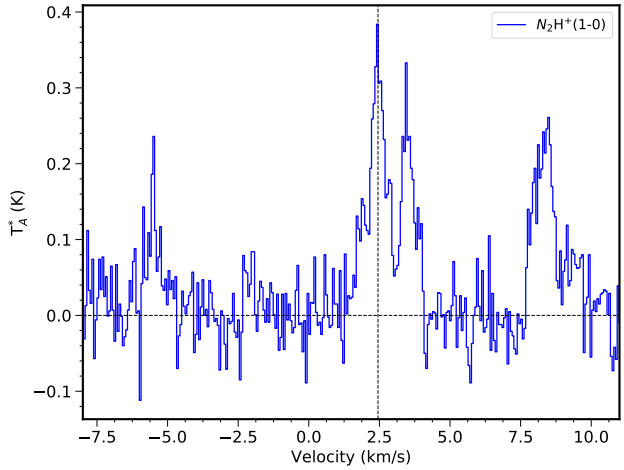

Figure 8. Average profile of N_2H^+ in blue over the clump. The vertical line shows the systematic velocity of the clump derived using a hyperfine fitting of the N_2H^+ line.

4.5.2. Gas Properties: Velocity Dispersion and Density

In this section, we discuss the line profile of the dense gas tracer N_2H^+ (1–0) and derive its properties to calculate the magnetic field strength of the cores. Dense gas tracers such as $C^{18}O$ and CS (2–1) are also commonly used for magnetic field strength estimation. Therefore, we also calculated B-field strength using $C^{18}O$ and CS (2–1) (see the Appendix) and compared it with the magnetic field strength estimated using the N_2H^+ line.

Figure 8 shows the spectrum of N_2H^+ (1–0) averaged over the clump in units of antenna temperature (K). The N_2H^+ line exhibits a hyperfine structure showing seven components, and we obtained the FWHM of the line by fitting Gaussians to the spectra. We fitted seven hyperfine components simultaneously with seven Gaussians, using the line parameters given by P. Caselli et al. (1995). For our analysis, we considered the velocity dispersion of the central bright component, which is representative of the cloud's systematic velocity. To derive the turbulent line width of the N_2H^+ tracer used in our magnetic field strength calculation, we corrected the measured line widths for thermal broadening with the following relation,

Table 1
DCF Results and Energetics Determined Using the N_2H^+ (1–0) Line

Core	$n(H_2)$ ($\times 10^4$ cm^{-3})	b (degrees)	$\sigma_{v,nt}$ (km s^{-1})	N_{turb}	B (μG)	λ	E_P[a] $\times 10^{39}$	E_G $\times 10^{42}$	E_B $\times 10^{42}$	$E_{outflow}$ $\times 10^{42}$	Type
21	11.5 ± 0.7	17.0 ± 1.7	0.26 ± 0.08	3.4	179 ± 50	0.6 ± 0.2	1.5	0.7	3.8	3.9	Starless
23	5.3 ± 0.4	17.0 ± 1.7	0.26 ± 0.08	3.4	121 ± 34	0.5 ± 0.1	2.3	1.6	2.8	5.9	Protostellar
24	8.1 ± 0.8	17.0 ± 1.7	0.26 ± 0.08	3.4	150 ± 42	0.6 ± 0.2	2.3	1.1	4.3	5.9	Protostellar

Note.
[a] Energy values are in the units of erg.

with the assumption that the total velocity dispersion is the summation of thermal and nonthermal contributions added in quadrature (P. C. Myers 1983),

$$\sigma_{nt} = \sqrt{(\sigma_{obs})^2 - (\sigma_{th})^2}, \quad (14)$$

where σ_{th} is $\sqrt{kT/\mu m_{obs}}$, thermal velocity dispersion; μ is the molecular weight of the observed N_2H^+ molecule; T is the gas temperature; and k is the Boltzmann constant. We used the dust temperature of the cores as the gas temperature to calculate the thermal line width. K. Pattle et al. (2017) derived the dust temperature for three cores in the range 21.8–23.5 K. Using the average $T_{dust} \sim 22.8$ K and the mean velocity dispersion of the central bright component as 0.28 ± 0.07 km s^{-1}, we calculated the nonthermal velocity dispersion as 0.26 ± 0.08 km s^{-1}. The beam size of the TRAO data ($\sim 56''$) is four times higher than that of JCMT, and the cores are not resolved at that angular scale. Therefore, we used the average value of nonthermal velocity dispersion for three cores. The gas density, $\rho = \mu_g m_H n(H_2)$, where $\mu_g = 2.8$ is the mean molecular weight of the gas, m_H is the mass of a hydrogen atom, and $n(H_2)$ is the number density of molecular hydrogen in cm^{-3}. We used the $n(H_2)$ estimates from K. Pattle et al. (2017), calculated using dust continuum emission, and the values for P17 21, P17 23, and P17 24 are $11.5 \pm 0.7 \times 10^4$ cm^{-3}, $5.3 \pm 0.4 \times 10^4$ cm^{-3}, and $8.1 \pm 0.8 \times 10^4$ cm^{-3}, respectively. We calculated N_{turb} for N_2H^+ spectra as 3.4 using the J. Cho & H. Yoo (2016) method described previously. Using the $n(H_2)$, σ_{nt} and b (shown in Table 1), we thus calculated the magnetic field strength for three cores using Equation (13).

We calculated the uncertainties in the B-field strength using the propagation of errors in the other quantities:

$$\delta B_{pos} = B_{pos}\sqrt{\left(\frac{1}{2}\frac{\delta n_{H_2}}{n_{H_2}}\right)^2 + \left(\frac{\delta\sigma_{nt}}{\sigma_{nt}}\right)^2 + \left(\frac{\delta b}{b}\right)^2}, \quad (15)$$

where $\delta n(H_2)$, $\delta\sigma_{nt}$, and δb are the uncertainties in the number density, nonthermal velocity dispersion, and polarization angle dispersion, respectively. Finally, we estimated the magnetic field strengths using the modified DCF method as 179 ± 50 μG, 121 ± 34 μG, and 150 ± 42 μG for P17 21, P17 23, and P17 24, respectively.

4.6. Mass-to-flux Ratio and Magnetic Criticality of the Clump

The stability of the clump can be assessed using the mass-to-flux ratio λ. $\lambda < 1$ implies that the clump is magnetically supported, while if $\lambda > 1$, it implies that the clump is unstable to gravitational collapse and is not well supported by the magnetic field. We estimated the mass-to-flux ratio (R. M. Crutcher 2004):

$$\lambda = 7.6 \times 10^{-21} \times N_{H_2}(\mathrm{cm}^{-2})/B_{pos}(\mu\mathrm{G}), \quad (16)$$

where N_{H_2} is the column density and B_{pos} is the plane-of-the-sky magnetic field strength. The dust column density values N_{H_2}, estimated using SCUBA emission, are $(13.7 \pm 0.9) \times 10^{21}$ cm^{-2}, $(7.3 \pm 0.6) \times 10^{21}$ cm^{-2}, and $(11.2 \pm 1.0) \times 10^{21}$ cm^{-2} for P17 21, P17 23, and P17 24, respectively (K. Pattle et al. 2017). Using these N_{H_2} and our B_{pos} estimates from N_2H^+ lines, we estimated λ as 0.6 ± 0.2, 0.5 ± 0.1, and 0.6 ± 0.2 for cores P17 21, P17 23, and P17 24, respectively. These values suggest that the starless P17 21 and protostellar cores, P17 23 and P17 24, are magnetically subcritical, implying that they are supported against gravitational collapse by their magnetic fields. However, it should be noted that two of the cores, P17 23 and P17 24, host embedded protostars and therefore are not stable. It is important to note that the values of λ qualitatively suggest the dynamical importance of magnetic fields in their evolution without precisely measuring the stability against collapse, and that our values of B-field strength might also be overestimated (K. Pattle et al. 2023).

5. Discussion

In this paper, we present magnetic field estimates in a reflection nebula triggered by an intermediate-mass star that acts as a bridge between low- and high-mass star-forming regions (A. Fuente et al. 1998b). The region of our study, NGC 7023, is a good example of triggered star formation having a pre-main sequence Herbig Ae Be star, HD 200775, as the central source which has triggered the formation of many dense condensations, some of which are forming young stellar objects (YSOs; J. M. Kirk et al. 2009). There is a biconical cavity in the east–west direction, which is likely to have been carved out by a bipolar outflow in an earlier evolutionary stage and is currently chemically inactive (A. Fuente et al. 1998b). The age of the central star HD 200775 is 1–3 Myr (M. Vioque et al. 2018), which is much longer than the lifetime of the Class I and Class II YSOs clustered around the hub with ages of around 0.1 Myr. The nebula can be considered a sheet of dense molecular gas in which a massive star is born and subsequently disperses the surrounding gas through radiative and stellar feedback. Pre-main-sequence stars with luminosities less than those of massive stars (F. Palla & S. W. Stahler 1993) cannot create extended H II regions; however, in several cases, extended atomic gas regions can be found associated with them (A. Fuente et al. 1998b). The pre-main-sequence star HD 200775, with bolometric luminosity $L_{bol} \sim 8000$ $L_\odot$ (M. E. van den Ancker et al. 1997) and mass 10 $M_\odot$, has

created three PDRs, or bright rims, located at the edges of the molecular cloud surrounding it and also the extended atomic regions (A. Fuente et al. 1998a). We focus on the clump located near PDR 1 (see the left panel of 1). The polarization observations using JCMT POL-2, with a linear scale of 0.024 pc, show an aligned magnetic field structure along the high-density structure (black skeleton in Figure 3). The magnetic field changes its orientation from being perpendicular at large scales (measured by Planck/optical) to parallel to the high-density structure at small scales (0.5–0.03 pc). However, the magnetic fields in the filamentary structures generally transition from being parallel to diffuse striations to being perpendicular to dense filaments (Planck Collaboration et al. 2016; E. Sharma et al. 2020). Therefore, the resultant geometry is inconsistent with both subcritical fields for the filament and subcritical fields that have evolved to be supercritical for the embedded cores. The self-gravity and magnetic fields are insufficient to explain the reordering of field lines along the clump morphology, and this hints toward the role of stellar feedback in regulating the dynamics of this high-density clump. Previous studies investigating the magnetic fields near PDRs in nearby and distant star-forming regions have identified similar reordered field structures (D. Ward-Thompson et al. 2017; J. Kwon et al. 2018; K. Pattle et al. 2018; J. Hwang et al. 2023; Z. A. Khan et al. 2024).

In addition, the resultant subcritical magnetic fields of two cores (see Section 4.6) with embedded protostars are not aligned with the theoretical expectation of gravitationally dominated collapsing cores. Given the presence of ongoing star formation, we expect the cores to be supercritical. It is possible that there are different physical processes responsible at clump and core scales. To understand the reasons behind this discrepancy, we further studied the energetics of the cores and discussed the possible scenarios that may arise at clump and core scales.

5.1. Energetic Analysis and the Possible Effect of Stellar Feedback on Polarization

To investigate the physical factors involved in the dynamics of the gas around C1, we estimated the energy budget of the cloud.

We calculated the magnetic energy (E_B) of the clump and compared it with other energy terms: gravitational (E_G), photon (E_P), and outflow (E_O) energies integrated over the whole region around it.

5.1.1. Magnetic Energy

We calculated the magnetic energy of the three cores as

$$E_B = \frac{4}{3}\pi R^3 B_{\rm pos}^2/8\pi, \tag{17}$$

where $B_{\rm pos}$ is the plane-of-sky magnetic field strength calculated from DCF analysis. We took the radii of the cores to be 0.029, 0.034, and 0.034 pc; these are deconvolved mean radii for the sources derived by K. Pattle et al. (2017) from their fitting of Gaussian models to emission peaks. The calculated magnetic energies are 3.8×10^{42} erg, 2.8×10^{42} erg, and 4.3×10^{42} erg for P17 21, 23, and 24, respectively.

5.1.2. Radiation Field Energy

We first estimated the total rate at which ionizing photons are emitted as $N_{\rm LyC} = 4\pi R^2 N_{\rm LyC}^0$, where the stellar radius is assumed to be 4.6 $R_\odot$, and then projected the number of Lyman continuum photons emitted on a per unit surface area to be $10^{20.4}$ cm^{-2} s^{-1}. The incident radiation field depends on the spectral type and the geometry of the ionizing star. The spectral type of HD 200775 is similar to HD 147889, and so we adopted the stellar properties—radius and Lyman continuum photons from K. Pattle et al. (2015).

We estimated the mean radiation energy from the ionizing photons emitted by the ionizing central star of spectral type B2V and penetrating the high-density cloud using the relation,

$$E_P = \frac{4R^2 k_{\rm B} T_{\rm HII}}{D_{\rm HII}} \left(\frac{3\pi N_{\rm LyC} R}{\alpha}\right)^{1/2}, \tag{18}$$

where $T_{\rm HII}$ is the canonical temperature of the gas in an H II region, and $D_{\rm HII}$ is the projected distance of the core from the central star. The projected distance of the clump from HD 200775 is 0.05 pc, assuming a distance of 340 pc (P. Saha et al. 2020). The calculated photon energies are 1.5×10^{39} erg, 2.3×10^{39} erg, and 2.3×10^{39} erg for P17 21, 23, and 24, respectively.

5.1.3. Gravitational Energy

We estimated the gravitational potential energy of the cores by assuming an axisymmetric ellipsoid using the relation,

$$E_G = -\frac{3}{5}\alpha\beta\frac{GM^2}{R}, \tag{19}$$

where $\alpha = (1 - b/3)/(1 - 2b/5)$ is the correction factor for elliptical cores with power-law density profile, $\rho = r^{-b}$, and $\beta = (\arcsin e)/e$ is the geometry factor (S. M. Fall & C. S. Frenk 1983; D. Li et al. 2013). We assume the typical density profile index for dense cores $b = 1.6$ (A. Palau et al. 2014), and β ranges from 1.0 to 1.4 with an average value of 1.2.

K. Pattle et al. (2017) estimated the masses of cores to be 0.50 $M_\odot$, 0.83 $M_\odot$, and 0.68 $M_\odot$ for P17 21, 23, and 24, respectively. We again took R to be the deconvolved radius of each core (see Section 5.1.1). Therefore the calculated gravitational energies are 0.7×10^{42} erg, 1.6×10^{42} erg, and 1.1×10^{42} erg for P17 21, 23, and 24, respectively.

5.1.4. Kinetic Energy of Outflowing Material

Figure 9 shows the Spitzer 8 μm emission map obtained from the *c2d* Spitzer Legacy project data release.[16] The magnetic field orientation toward the clump is visible at the periphery of the reflection nebula (dotted lines in cyan). The clump's location and the nebula's geometry suggest that the outflow from the central source has significantly reshaped the clump. The systematic velocity of the nebula using $C^{18}O$ (1–0) averaged over the whole nebula is $\sim$2.7 km s^{-1} (E. Sharma et al. 2025, in preparation). Figure 10 shows the distribution of high-velocity gas in the red- and blueshifted wings, which is overplotted on the Herschel dust column density map of

[16] http://ssc.spitzer.caltech.edu/legacy/c2dhistory.html

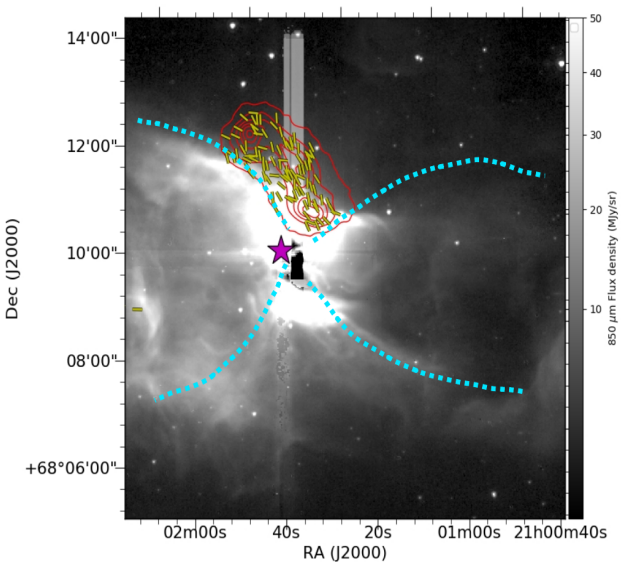

Figure 9. Spitzer 8 μm emission map of NGC 7023 taken from the *c2d* catalog (N. J. Evans et al. 2003). The red contours and yellow vectors show the SCUBA-2 emission contours and the magnetic field orientation derived from our POL-2 measurements, respectively. The dotted cyan curves mark the outer periphery of the biconical structure of the nebula, and the magenta star shows the central source HD 200775. The extent of the emission region around HD 200775 corresponds to the yellow box marked in Figure 10.

NGC 7023. To understand the effect of outflow on the clump energetics, we estimated the outflow kinetic energy using the ^{12}CO (1–0) emission in the high-velocity ranges of 4–5 km s^{-1} and 5–7.5 km s^{-1}. Then, we considered its possible contribution to the energy balance of each of the three cores. The H_2 mass and the kinetic energy $\frac{1}{2}M_{\rm outflow}v^2$ are calculated to be $\sim$ 37 $M_\odot$ and 1.6×10^{45} erg in the velocity range of 4–5 km s^{-1}, and 29 $M_\odot$ and 6.2×10^{45} erg in the range of 5–7.5 km s^{-1}. A. Fuente et al. (1998b) modeled the outflow as a pair of cones, each of diameter 0.9 pc and slant height 1 pc. Again, adjusting for the difference in assumed distance, this is equivalent to a surface area of 1.28 pc^2. We assume that the energy of the outflow is distributed evenly over this surface area, although we note that this likely results in an underestimate of the true energy incident on our cores, as they are very close to the exciting star. K. Pattle et al. (2017) derived FWHMs for the three cores of 0.029, 0.035, and 0.035 pc. The areas projected by these three cores onto the cone are taken to be $\pi \times (\mathrm{FWHM}/2)^2$, 0.052%, 0.075%, and 0.075% of the total surface area, respectively. Thus we estimate outflow kinetic energies incident on the cores of $\gtrsim 4 \times 10^{42}$ erg for core P17 21, and $\gtrsim 6 \times 10^{42}$ erg for cores P17 23 and P17 24. The outflow kinetic energies for the three cores are comparable to their respective gravitational and magnetic energies in the clump.

Figure 11 shows a schematic of NGC 7023, summarizing the suggested scenario with the B-field structure toward C1 and the outflow feedback through high-velocity gas as shown. The dashed yellow lines show the B-field geometry of the clump (with marked cores in black), which is perpendicular to the direction of the ionization radiation. A. Fuente et al. (1996) showed the high-density filaments/clumps around the bipolar outflow could have been created by its interaction with the surrounding cloud. Using the hydrodynamic simulations of magnetized clouds under the radiative feedback, S. J. Arthur et al. (2011) showed that the H II region sweeps the material while expanding due to the bow shock front. This expansion of the H II region compresses the high-density gas, dragging the magnetic field lines due to flux freezing conditions and aligning the magnetic field along the high-density clump. J. Mackey & A. J. Lim (2011) also further investigated the structural transformation of globules with different magnetic field strengths, where the initially perpendicular B-field will get altered and enhanced. Recent simulations by G. Granda-Muñoz et al. (2025) have also studied the evolution of magnetic fields' geometry in the presence of stellar feedback, and our results agree with their simulations. Expansion of H II regions and the compression of the molecular gas in the surrounding cloud thus helps increase the density of the clump, thereby inducing the fragmentation of the cloud. We suggest that the reordered and enhanced B-field strength of C1 in NGC 7023 is a consequence of outflow feedback (see Figures 9 and 10), where the initially weak B-fields get compressed through PDR expansion and the B-field strength is thus amplified ($\sim$150–179 μG) in clump C1.

However, it is also important to note that the gravitational and outflow energies of each core are comparable to their respective magnetic energies, which suggests that the system is near dynamical equilibrium with an ongoing star formation in two cores, P17 23 and P17 24. We suggest that the magnetic pressure in C1 would keep increasing in a contrary response to the expanding inward momentum of the PDR layers until the energies are comparable and the system attains equilibrium. This prevents further dissociation due to stellar feedback and maintains the evolution of the clump in a strong field regime. In addition, the magnetic field strengths are also likely to be systematically overestimated (K. Pattle et al. 2023), which will affect the estimation of the magnetic energies of the cores. While we have used the J. Cho & H. Yoo (2016) method to correct the magnetic field strength, J. Liu et al. (2021) suggested that this method can only account for the effect of line-of-sight integration on size scales larger than 0.1 pc. The role of the B-field thus might be dominant only at the clump scales but subdominant in affecting the cores' stability against gravitational collapse. Future high-resolution polarization observations toward the cores will help gain insights into the role of magnetic fields in cores' stability.

6. Conclusions

We have presented polarized 850 μm dust emission observations of the reflection nebula NGC 7023, also known as the Iris nebula, using the POL-2 polarimeter on the JCMT. We found reordered magnetic fields parallel to the high-density structure. We modeled the relationship between the polarization fraction and dust emission intensity. We found the power index to be 0.65, which implies a decrease in the dust grain alignment efficiency with increasing A_V. We also compared our POL-2 results with previous starlight and Planck dust polarization, and found that POL-2 shows a completely different distribution of polarization vectors, suggesting a different physical mechanism influencing the magnetic field on smaller scales within the nebula. The magnetic field strengths are estimated using N_2H^+ lines observed with the TRAO telescope, and the calculated values are 179 ± 50 μG, 121 ± 34 μG, and 150 ± 42 μG for P17 21,

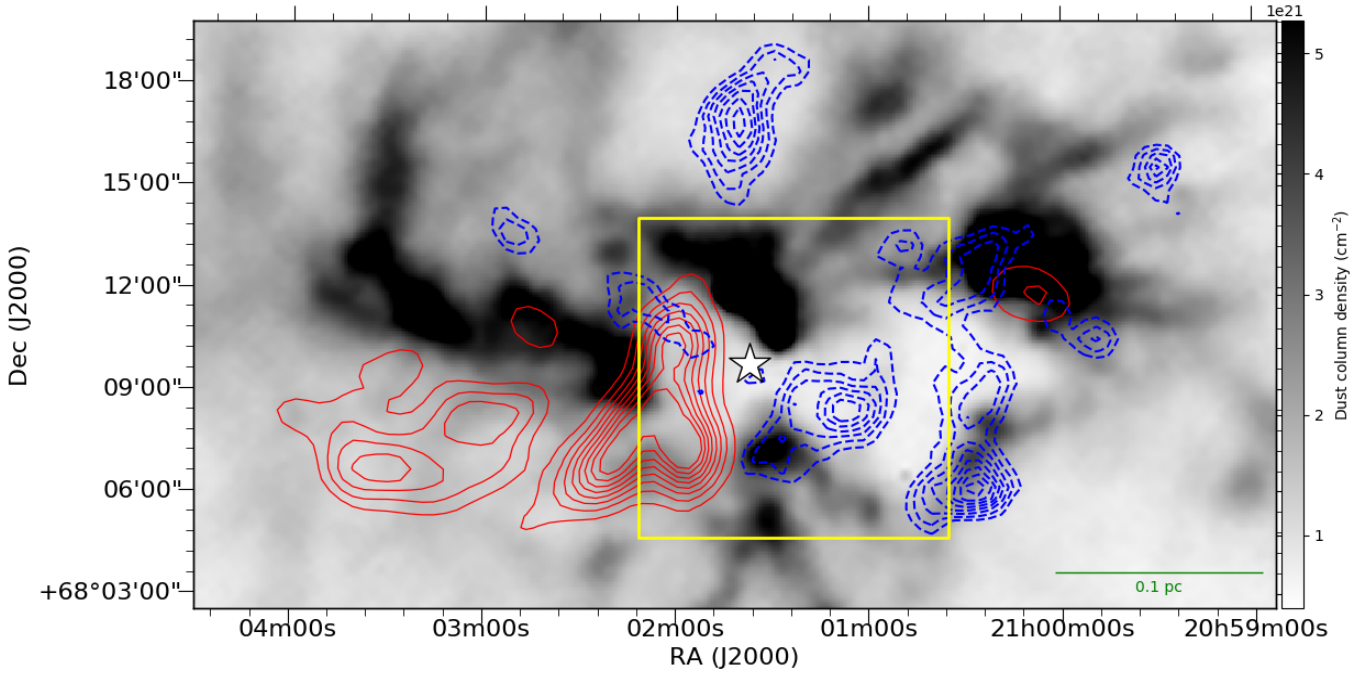

Figure 10. Herschel dust column density map of the region with red- and blueshifted high-velocity ^{12}CO gas around the star. The red contours show the integrated ^{12}CO emission in the velocity range 5–7.5 km s^{-1} and blue dotted contours in the velocity interval −2.5 to 0 km s^{-1}. The contour levels for red contours range from 1.25 to 7 K km s^{-1} in steps of 5σ with σ as 0.15 K km s^{-1}, and for blueshifted gas, the levels range from 1.3 to 6 K km s^{-1} in steps of 3σ ($\sigma \sim 0.18$ K km s^{-1}). The yellow box marks the extent of the Spitzer data shown in Figure 9. The systematic velocity of the cloud is ∼2.7 km s^{-1}.

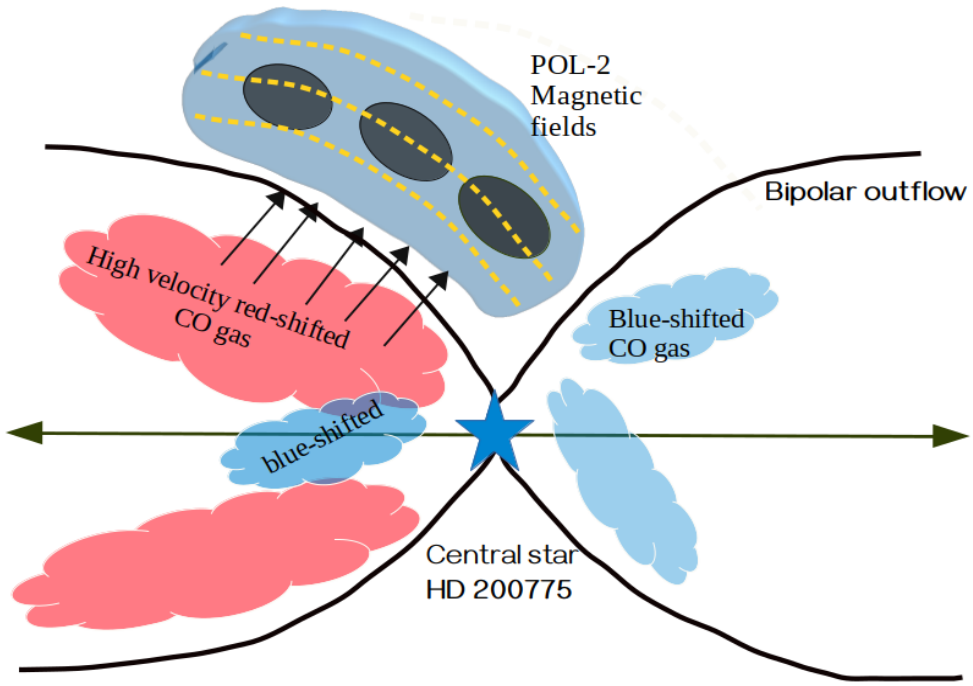

Figure 11. Schematic view of the clump C1 in the NGC 7023 region. Black solid lines show the bipolar outflow, and the double arrow shows the direction of the outflow axis. The central source HD 200775 is marked by a blue star. The black ellipses show three cores in the blue-colored clump. The dashed lines show the derived magnetic field direction in the clump using POL-2. Black arrows show the direction of the compression across the outflow walls. The red and blue structures show the red- and blueshifted gas traced in outflow wings.

P17 23, and P17 24, respectively. Both the protostellar cores, P17 23 and P17 24, and the starless core, P17 21, are magnetically subcritical, implying the dominating role of magnetic fields, but the ongoing star formation in the cores suggests our magnetic field strengths might be overestimated.

We found that the three cores are embedded in a filamentary structure that is curved around the upper-left wall of the outflow cavity formed by the Herbig Ae/Be star HD 200775, and that the magnetic field is aligned parallel to the length of the filament and the outflow cavity wall, inconsistent with predictions of magnetic field geometries for self-gravitating cores in dense filaments. Our energetic analysis suggests that the energy impinging on the cores due to the outflow is comparable to their gravitational and magnetic energies. We therefore conclude that the B-fields in the clump have been compressed and reordered by outflow feedback.

Acknowledgments

This work is supported by the National Natural Science Foundation of China (NSFC; grant Nos. 12588202 and 11988101) and by the Alliance of International Science Organizations (grant No. ANSO-VF-2021-01). We are grateful to the anonymous referee for their valuable comments that have improved the presentation of this paper. D.L. is a new cornerstone investigator. K.P. is a Royal Society University Research Fellow, supported by grant No. URF\R1\211322. C. W.L. acknowledges support from the Basic Science Research Program through the National Research Foundation of Korea (NRF), funded by the Ministry of Education, Science and Technology (NRF- 2019R1A2C1010851), and from the Korea Astronomy and Space Science Institute grant funded by the Korean government (MSIT; project No. 2024-1-841-00). The James Clerk Maxwell Telescope is operated by the East Asian Observatory on behalf of the National Astronomical Observatory of Japan; the Academia Sinica Institute of Astronomy and Astrophysics; the Korea Astronomy and Space Science Institute; the National Astronomical Research Institute of Thailand; the Center for Astronomical Mega-Science (as well as the National Key R&D Program of China with grant No. 2017YFA0402700). Additional funding support is provided by the Science and Technology Facilities Council of the United Kingdom and participating universities and organizations in the United Kingdom, Canada, and Ireland. Additional funds for the construction of SCUBA-2 were provided by the Canada Foundation for Innovation. The authors wish to recognize and acknowledge the very significant cultural role and reverence that the summit of Maunakea has always had within the Indigenous Hawaiian community. We are most fortunate to have the opportunity to conduct observations from this mountain. This research has made use of the NASA/IPAC Infrared Science Archive, which is funded by the National Aeronautics and Space Administration and operated by the California Institute of Technology.

Appendix
Comparison of DCF Strengths for Three Tracers N_2H^+ (1–0), $C^{18}O$ (1–0) and CS (2–1)

The N_2H^+ lines trace the deepest regions of the core, as the critical density is higher for N_2H^+ ($n \sim 10^6$ cm^{-3}). At the same time, $C^{18}O$ and CS (2–1) lines, being the dense gas tracers, are also commonly used to estimate the magnetic field strength. However, the magnetic field strength is expected to vary with the use of different tracers pertaining to their different optical depths (C. Yin et al. 2021). To understand this variation with different gas tracers, we compared the line profiles and velocity dispersions of $C^{18}O$ and CS (2–1) lines with those of N_2H^+, and further calculated the magnetic field strength (Table 2). The correlation of dust and molecular line analysis shown in Figure 12 also shows the N_2H^+ (1–0) line as the best possible tracer for the field strength calculation, as it correlates well with the dust continuum emission (F. D. Priestley et al. 2024).

Figure 13 shows the comparison of the spectra of the three tracers, $C^{18}O$ (1–0), CS (2–1), and N_2H^+ (1–0), averaged over the clump morphology in units of antenna temperature (K). We estimated the velocity dispersion of three different molecular lines using the Gaussian fitting of $C^{18}O$ (1–0) and CS (2–1), and the hyperfine fitting of N_2H^+ lines. The mean FWHMs of the $C^{18}O$ and CS (2–1) lines are 1.2 and 1.8 km s^{-1}, respectively.

Table 2 shows the calculated magnetic field strengths, estimated using three tracers, and the estimated strength varies by a factor of two. We further compared the integrated line emission of three tracers with the dust continuum emission obtained with SCUBA-2 to understand the effect of different tracers for estimating magnetic field strength. Figure 12 shows the SCUBA-2 dust emission maps of NGC 7023 with the overplotted molecular line emission contours for the N_2H^+ (1–0), $C^{18}O$ (1–0), and CS (2–1) lines. The contours show the integrated intensity maps of molecular lines. We find that the gas and dust emissions are more morphologically correlated for N_2H^+ in panel (a). Therefore, the dust emission and gas traced by an optically thin tracer, N_2H^+ (1–0), effectively represent the same layer of cloud. This also confirms the use of the N_2H^+ (1–0) line to estimate the magnetic field strength in our calculations.

Table 2
Comparison of Magnetic Field Strength for Three Line Tracers

Core	$n(H_2)$ ($\times 10^4$ cm^{-3})	b (degrees)	N_2H^+			CS			$C^{18}O$		
			$\sigma_{v,nt}$ (km s^{-1})	$N_{\rm turb}$	B (μG)	$\sigma_{v,nt}$ (km s^{-1})	$N_{\rm turb}$	B (μG)	$\sigma_{v,nt}$ (km s^{-1})	$N_{\rm turb}$	B (μG)
21	11.5 ± 0.7	17.0 ± 1.7	0.26 ± 0.08	3.4	179 ± 50	0.33 ± 0.03	12.1	118 ± 15	0.31 ± 0.03	15.1	100 ± 14
23	5.3 ± 0.4	17.0 ± 1.7	0.26 ± 0.08	3.4	121 ± 34	0.33 ± 0.03	12.1	80 ± 11	0.31 ± 0.03	15.1	68 ± 10
24	8.1 ± 0.8	17.0 ± 1.7	0.26 ± 0.08	3.4	150 ± 42	0.33 ± 0.03	12.1	99 ± 13	0.31 ± 0.03	15.1	84 ± 12

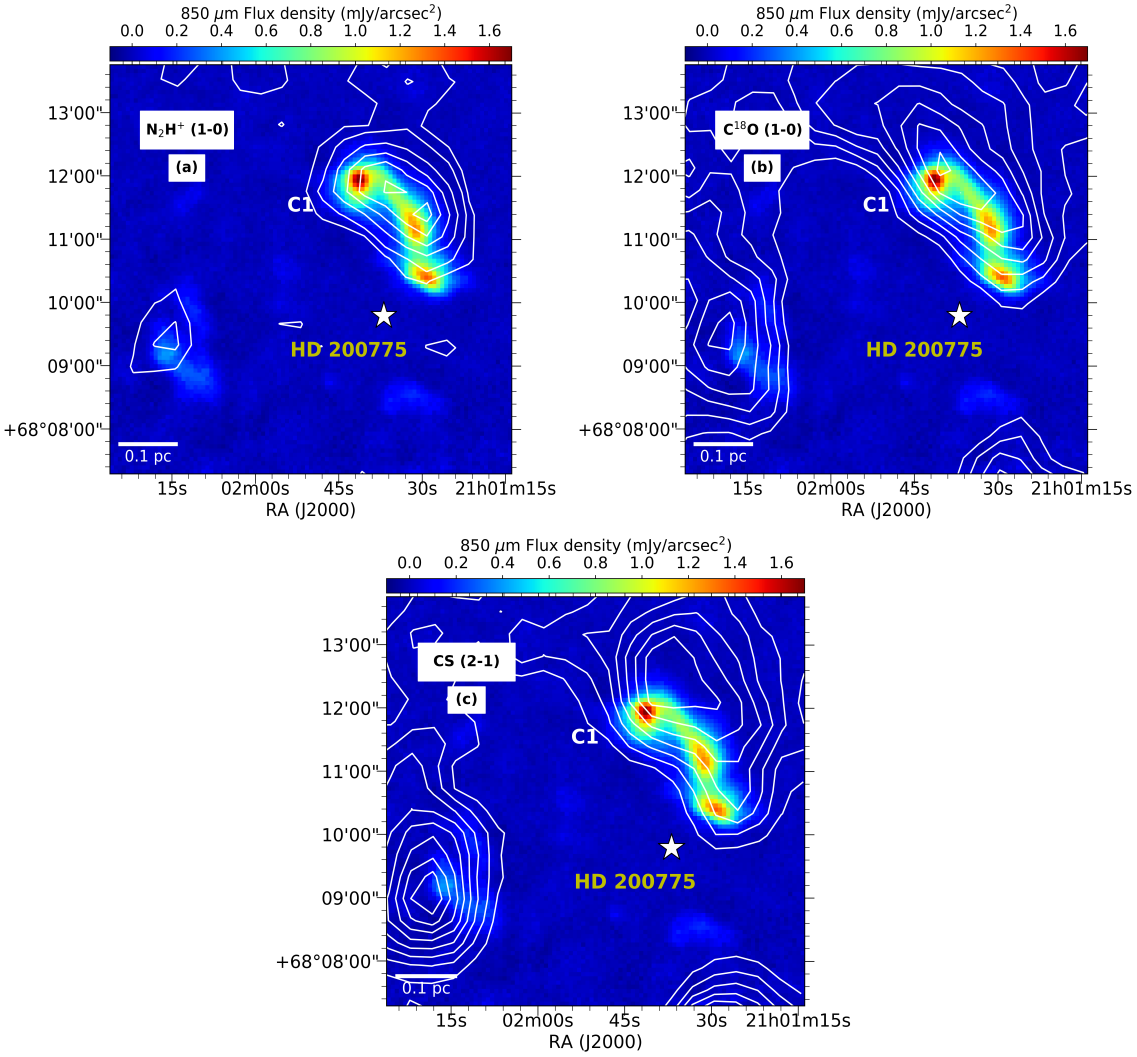

Figure 12. SCUBA-2 dust continuum emission maps of the observed region with overplotted molecular line emission contours for (a) N_2H^+ (1–0), with the contour levels ranging from 0.5 to 1.3 K km s^{-1} in steps of ∼0.1 K km s^{-1}; (b) $C^{18}O$ (1–0) line with the contour levels ranging from 0.3 to 1.3 K km s^{-1} in steps of 0.14 K km s^{-1}; (c) CS(2–1) with the contour levels ranging from 0.2 to 0.8 K km s^{-1} in steps of ∼0.1 K km s^{-1}.

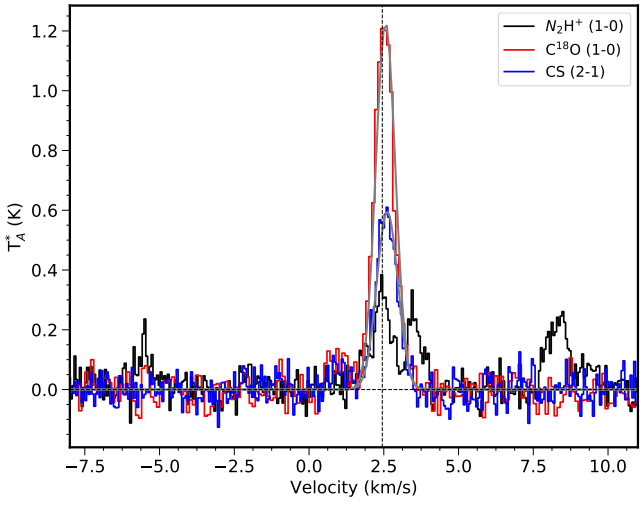

Figure 13. Average profiles of N_2H^+ in black, $C^{18}O$ in red, and CS (2–1) in blue toward the clump. The gray lines show the fitted Gaussians. The vertical line shows the systematic velocity of the clump derived using a hyperfine fitting of the N_2H^+ line.

ORCID iDs

Ekta Sharma https://orcid.org/0000-0002-4541-0607
Kate Pattle https://orcid.org/0000-0002-8557-3582
Di Li https://orcid.org/0000-0003-3010-7661
Chang Won Lee https://orcid.org/0000-0002-3179-6334
Maheswar Gopinathan https://orcid.org/0009-0007-0745-9147
Tao-Chung Ching https://orcid.org/0000-0001-8516-2532
Mehrnoosh Tahani https://orcid.org/0000-0001-8749-1436
Shinyoung Kim https://orcid.org/0000-0001-9333-5608

References

Alecian, E., Catala, C., Wade, G. A., et al. 2008, MNRAS, 385, 391
Alves, F. O., Frau, P., Girart, J. M., et al. 2014, A&A, 569, L1
Andersson, B. G., Lazarian, A., & Vaillancourt, J. E. 2015, ARA&A, 53, 501
Arthur, S. J., Henney, W. J., Mellema, G., de Colle, F., & Vázquez-Semadeni, E. 2011, MNRAS, 414, 1747
Beck, R. 2015, A&ARv, 24, 4
Caselli, P., Benson, P. J., Myers, P. C., & Tafalla, M. 2002, ApJ, 572, 238
Caselli, P., Myers, P. C., & Thaddeus, P. 1995, ApJL, 455, L77
Chandrasekhar, S., & Fermi, E. 1953, ApJ, 118, 113

Chapin, E. L., Berry, D. S., Gibb, A. G., et al. 2013, MNRAS, 430, 2545
Chen, Z., Sefako, R., Yang, Y., et al. 2022, RAA, 22, 075017
Ching, T.-C., Qiu, K., Li, D., et al. 2022, ApJ, 941, 122
Cho, J., & Yoo, H. 2016, ApJ, 821, 21
Crutcher, R. M. 2004, Ap&SS, 292, 225
Crutcher, R. M. 2012, ARA&A, 50, 29
Davis, L. 1951, PhRv, 81, 890
Davis, L., Jr, & Greenstein, J. L. 1951, ApJ, 114, 206
di Francesco, J., Evans, N. J., II, Caselli, P., et al. 2007, in Protostars and Planets V, ed. B. Reipurth, D. Jewitt, & K. Keil (Tucson, AZ: Univ. Arizona Press), 17
Di Francesco, J., Keown, J., Fallscheer, C., et al. 2020, ApJ, 904, 172
Eswaraiah, C., Li, D., Samal, M. R., et al. 2020, ApJ, 897, 90
Evans, N. J., II, Allen, L. E., Blake, G. A., et al. 2003, PASP, 115, 965
Fall, S. M., & Frenk, C. S. 1983, AJ, 88, 1626
Friberg, P., Bastien, P., Berry, D., et al. 2016, Proc. SPIE, 9914, 991403
Fuente, A., Martin-Pintado, J., Bachiller, R., Neri, R., & Palla, F. 1998a, A&A, 334, 253
Fuente, A., Martin-Pintado, J., Neri, R., Rogers, C., & Moriarty-Schieven, G. 1996, A&A, 310, 286
Fuente, A., Martin-Pintado, J., Rodriguez-Franco, A., & Moriarty-Schieven, G. D. 1998b, A&A, 339, 575
Granda-Muñoz, G., Vázquez-Semadeni, E., & Gómez, G. C. 2025, A&A, 694, A296
Henning, T., Wolf, S., Launhardt, R., & Waters, R. 2001, ApJ, 561, 871
Hildebrand, R. H., Kirby, L., Dotson, J. L., Houde, M., & Vaillancourt, J. E. 2009, ApJ, 696, 567
Hoang, T., Tram, L. N., Lee, H., Diep, P. N., & Ngoc, N. B. 2021, ApJ, 908, 218
Holland, W. S., Bintley, D., Chapin, E. L., et al. 2013, MNRAS, 430, 2513
Hollenbach, D. J., & Tielens, A. G. G. M. 1997, ARA&A, 35, 179
Hwang, J., Kim, J., Pattle, K., et al. 2022, ApJ, 941, 51
Hwang, J., Pattle, K., Parsons, H., Go, M., & Kim, J. 2023, AJ, 165, 198
IAU 1973, Transactions of the IAU, Vol. 15 (Cambridge: Cambridge Univ. Press), 165
Jones, T. J., Bagley, M., Krejny, M., Andersson, B. G., & Bastien, P. 2015, AJ, 149, 31
Khan, Z. A., Pattle, K., & Graves, S. F. 2024, MNRAS, 535, 107
Kirk, J. M., Ward-Thompson, D., Di Francesco, J., et al. 2009, ApJS, 185, 198
Koch, E. W., & Rosolowsky, E. W. 2015, MNRAS, 452, 3435
Köhler, M., Habart, E., Arab, H., et al. 2014, A&A, 569, A109
Krumholz, M. R., & Federrath, C. 2019, FrASS, 6, 7
Kwon, J., Doi, Y., Tamura, M., et al. 2018, ApJ, 859, 4
Kwon, W., Pattle, K., Sadavoy, S., et al. 2022, ApJ, 926, 163
Lazarian, A., & Hoang, T. 2007, MNRAS, 378, 910
Lê, N., Tram, L. N., Karska, A., et al. 2024, A&A, 690, A191
Lee, C. W., Myers, P. C., & Tafalla, M. 2001, ApJS, 136, 703
Li, D., Kauffmann, J., Zhang, Q., & Chen, W. 2013, ApJL, 768, L5
Liu, J., Zhang, Q., Commerçon, B., et al. 2021, ApJ, 919, 79
Mackey, J., & Lim, A. J. 2011, MNRAS, 412, 2079
Magakian, T. Y. 2003, A&A, 399, 141
Mairs, S., Dempsey, J. T., Bell, G. S., et al. 2021, AJ, 162, 191
Montier, L., Plaszczynski, S., Levrier, F., et al. 2015, A&A, 574, A136
Motte, F., Bontemps, S., & Louvet, F. 2018, ARA&A, 56, 41
Myers, P. C. 1983, ApJ, 270, 105
Myers, P. C. 2009, ApJ, 700, 1609
Palau, A., Estalella, R., Girart, J. M., et al. 2014, ApJ, 785, 42
Palla, F., & Stahler, S. W. 1993, ApJ, 418, 414
Pattle, K., Fissel, L., Tahani, M., Liu, T., & Ntormousi, E. 2023, in APS Conf. Ser. 534, Protostars and Planets VII, ed. S. Inutsuka et al. (San Francisco, CA: ASP), 193
Pattle, K., Ward-Thompson, D., Hasegawa, T., et al. 2018, ApJL, 860, L6
Pattle, K., Ward-Thompson, D., Kirk, J. M., et al. 2015, MNRAS, 450, 1094
Pattle, K., Ward-Thompson, D., Kirk, J. M., et al. 2017, MNRAS, 464, 4255
Pattle, K., Lai, S.-P., Di Francesco, J., et al. 2021, ApJ, 907, 88
Pattle, K., Lai, S.-P., Hasegawa, T., et al. 2019, ApJ, 880, 27
Pereyra, A., & Magalhães, A. M. 2007, ApJ, 662, 1014
Planck Collaboration, Ade, P. A. R., Aghanim, N., et al. 2016, A&A, 586, A138
Plaszczynski, S., Montier, L., Levrier, F., & Tristram, M. 2014, MNRAS, 439, 4048
Priestley, F. D., Clark, P. C., Glover, S. C. O., et al. 2024, MNRAS, 531, 4408
Saha, P., Gopinathan, M., Kamath, U., et al. 2020, MNRAS, 494, 5851
Saha, P., Gopinathan, M., Sharma, E., et al. 2021, A&A, 655, A76
Serkowski, K. 1962, AdA&A, 1, 289
Sharma, E., Gopinathan, M., Soam, A., Lee, C. W., & Seshadri, T. R. 2022, MNRAS, 517, 1138
Sharma, E., Gopinathan, M., Soam, A., et al. 2020, A&A, 639, A133
Shirley, Y. L. 2015, PASP, 127, 299
Soam, A., Maheswar, G., Lee, C. W., Neha, S., & Andersson, B.-G. 2017, MNRAS, 465, 559
Soam, A., Pattle, K., Ward-Thompson, D., et al. 2018, ApJ, 861, 65
Soler, J. D., Hennebelle, P., Martin, P. G., et al. 2013, ApJ, 774, 128
Steiman-Cameron, T. Y., Haas, M. R., Tielens, A. G. G. M., & Burton, M. G. 1997, ApJ, 478, 261
Tahani, M., Bastien, P., Furuya, R. S., et al. 2023, ApJ, 944, 139
van den Ancker, M. E., The, P. S., Tjin A Djie, H. R. E., et al. 1997, A&A, 324, L33
Vioque, M., Oudmaijer, R. D., Baines, D., Mendigutía, I., & Pérez-Martínez, R. 2018, A&A, 620, A128
Ward-Thompson, D., Kirk, J. M., Crutcher, R. M., et al. 2000, ApJL, 537, L135
Ward-Thompson, D., Pattle, K., Bastien, P., et al. 2017, ApJ, 842, 66
Whittet, D. C. B., Hough, J. H., Lazarian, A., & Hoang, T. 2008, ApJ, 674, 304
Yin, C., Priestley, F. D., & Wurster, J. 2021, MNRAS, 504, 2381
Zinnecker, H., & Yorke, H. W. 2007, ARA&A, 45, 481